# Elongation of gold nanoparticles in silica glass by irradiation with swift heavy ions

Koichi Awazu,[*] Xiaomin Wang, Makoto Fujimaki, and Junji Tominaga

*Center for Applied Near-field Optics Research, AIST, 1-1-1 Higashi Tsukuba 305-8562, Japan*

Hirohiko Aiba and Yoshimichi Ohki

*Department of Electrical Engineering and Bioscience, Waseda University, Shinjuku, Tokyo 169-8555, Japan*

Tetsuro Komatsubara

*Tandem Accelerator Complex, University of Tsukuba, Tsukuba 305-8577, Japan*
(Received 6 April 2008; published 6 August 2008; corrected 19 August 2008)

We examined the mechanism whereby nanoparticles of gold embedded in silica become elongated and oriented parallel to each other on ion irradiation. Elongation occurred for gold particles with radii smaller than 25 nm. The process was simulated by using a thermal spike model. For small-radius nanoparticles, ion irradiation raises the temperature above the melting points of both gold and silica, whereas for larger nanoparticles neither the gold nanoparticle nor the surrounding silica matrix is melted.

## I. INTRODUCTION

One-dimensional metallic nanostructures such as nanorods have important applications in sensing and photonics.[1] Shape anisotropy introduces new optical properties in Au nanoparticles, such as the presence of longitudinal plasmon resonance bands in the visible spectrum.[2] Thanks to efforts of several groups, the surfactant-directed synthesis of one-dimensional Au nanostructures is a well-developed technique.[3,4] Spherical Au nanoparticles show a single plasmon absorption band at 510 nm that is relatively independent of the size of the particles.[2] Au nanorods, on the other hand, show two principle plasmon bands. The shorter-wavelength band corresponds to absorption and scattering of light along the short axis of the nanorods (transverse plasmon band), and the band at longer wavelengths corresponds to absorption and scattering of light along the long axis of the nanorods (longitudinal plasmon band). The plasmon absorption bands can be tuned from visible wavelengths to near-IR wavelengths by adjusting the aspect ratio of the nanorods.

Au nanoparticles or nanorods can be deposited randomly on a substrate, but it is difficult to synthesize Au nanorods that are oriented parallel to each other and perpendicular to the substrate. Anisotropic metal colloids can be fabricated controllably by irradiating colloidal particles, each consisting of a Au core surrounded by a silica shell, with ions of megaelectron volt (MeV) energies at 77 K.[5,6] We hypothesized that optical losses could be reduced by fabricating an array of Au nanorods with their long axes aligned parallel to the direction of light propagation. Recently, fabrication by using ion beams was examined as a means of controlling the size and spatial distribution of Au nanorods.[7–12] During ion bombardment, however, uncontrolled nucleation and growth processes resulted in broad spatial and size distributions of the resulting nanoparticles. Nanoparticles of Co in SiO$_2$ showed some elongation with their long axes aligned in the direction of the ion beam; in contrast, Ge nanoparticles in SiO$_2$ were collapsed with their short axes aligned in the direction of the ion beam.[13,14]

In the present work, we found that the elongation of Au nanoparticles under ion irradiation depends on the size of the nanoparticles and electronic-stopping power of the ion beam at room temperature. Elongation of Au nanoparticles was observed in cases when both the SiO$_2$ matrix and the embedded Au nanoparticles were melted by the passage of an ion. On the basis of the present work, it should be possible to control the size of Au nanorods to produce new optical devices, such as nonlinear optics or optics with a negative refractive index.

## II. EXPERIMENT

### A. Fabrication of aligned Au nanorods in SiO$_2$

A thermally oxidized silicon wafer was prepared as a SiO$_2$ substrate; the thickness of the SiO$_2$ layer on the silicon was 2 $\mu$m. A 5-nm-thick Au film was deposited on the substrate by evaporation of high-purity Au grains. After deposition, the thin Au film was heated at 300 or 1 000 °C for 10 min to form Au nanoparticles: the particle size depended on the heating temperature. The Au nanoparticles were then embedded in a SiO$_2$ layer deposited by radio-frequency magnetron sputtering of a silica target in an Ar atmosphere. The thickness of the top layer of SiO$_2$ was 1 $\mu$m. The direction of propagation of the ion beam was perpendicular to the upper surface of the SiO$_2$. The 12-unit double-Pelletron tandem accelerator at the University of Tsukuba was used to irradiate the assemblies with 110 MeV Br$^{10+}$, 100 MeV Cu$^{9+}$, or 90 MeV Cl$^{8+}$ ions. A plan view of the deposited Au nanoparticles on SiO$_2$ was observed by field-emission scanning electric microscopy (FE-SEM) using a 20 kV Hitachi S-4800 instrument. Cross sections of the pristine and irradiated samples were examined by transmission electric microscopy (TEM) using a Hitachi H-9500 300 kV instrument. Specimens for TEM observation with a thickness of 100 nm were produced by using a focused beam of 20 keV Ga$^+$ ions from a Hitachi FB-2100 instrument.

### B. Simulation based on the thermal spike model

To simulate the thermal evolution around nanoparticles being irradiated by swift heavy ions, we adopt the thermal

TABLE I. The fitted lattice specific heat $C$ and thermal conductivity $K$ of gold and silica used in the simulation.

| Materials Ref. [ ] | Temperature range [K] | Lattice specific heat [J/g K] and Thermal conductivity [W/K cm] |
|---|---|---|
| Au [24] | 0−298.15 | $C=0.12966/(5296.47711/T^{2.24133}+1.0)$ |
| [26] | 298.15−900 | $C=0.118504+3.075801\times10^{-5}\ T-5.994305$ $\times10^{-9}\ T^2+1.211615\times10^2/T^2$ |
| | 900−$T_m$ $T_m$−1600 | $C=0.817819-9.157044\times10^{-4}\ T+3.580853$ $\times10^{-7}\ T^2-1.152968\times10^5/T^2$ |
| | 1600−$T_v$ $T_v$−5000 | $C=-1.364746+1.204728\times10^{-3}\ T-2.682983$ $\times10^{-7}\ T^2+7.206217\times10^5/T^2$ |
| | 5000−10000 | $C=0.153152+2.359460\times10^{-6}\ T-3.826152$ $\times10^{-10}\ T^2+3.617839\times10^3/T^2$ |
| [25] | 0−15 | $C=0.070401+3.581703\times10^{-5}\ T-3.698613$ $\times10^{-9}\ T^2-9.297549\times10^4/T^2$ |
| | 15−300 300−$T_m$ | $C=0.237455-1.534712\times10^{-5}\ T+6.164356$ $\times10^{-10}\ T^2-5.767945\times10^5/T^2$ |
| | $T_m$−9500 | $K=0.04112+4.1561\ T+0.2118\ T^2-0.05171\ T^3$ $+0.00172\ T^4$ |
| | | $K=3.17082+21.69108\ e^{(13.55947-T)/9.32813}$ $+0.99236\ e^{(13.55947-T)/66.82603}$ |
| | | $K=3.194-3.72302\times10^{-5}\ T-3.74366\times10^{-7}\ T^2$ |
| | | $K=0.39857+7.11481\times10^{-4}\ T-1.90481$ $\times10^{-7}\ T^2+1.78974\times10^{-11}\ T^3-6.52785$ $\times10^{-16}\ T^4$ |
| SiO$_2$ [23] | 100−273 | $C=-0.04764+0.00358\ T-3.11229\times10^{-6}\ T^2$ |
| [24] | 273−$T_m$ | $C=0.89193+3.11479\times10^{-4}\ T-21043.99319/T^2$ |
| [18] | $T>T_m$ | $C=1.42753$ |
| [25] | 0−10 | $K=-1.29614\times10^{-7}+1.86779\times10^{-4}\ T+7.32051$ $\times10^{-5}\ T^2-1.95377\times10^{-5}\ T^3+1.55681$ $\times10^{-6}\ T^4-3.94851\times10^{-8}\ T^5$ |
| | 10−200 | $K=0.0012-1.10697\times10^{-5}\ T+1.71903\times10^{-6}\ T^2$ $-1.55025\times10^{-8}\ T^3+5.95265\times10^{-11}\ T^4$ $-8.61625\times10^{-14}\ T^5$ |
| | 200−1400 | $K=-0.00524+1.46844\times10^{-4}\ T-4.3031$ $\times10^{-7}\ T^2+6.26894\times10^{-10}\ T^3-4.22469$ $\times10^{-13}\ T^4+1.12989\times10^{-16}\ T^5$ |
| | $T>1400$ | $K=0.02$ |

spike model,[15] which we extended to permit simultaneous modeling of multiphase materials because good agreement between simulated predictions and the experimental data have been shown in many reports. However, Coulomb explosion model have been often treated as competing models for describing ion irradiation effects because weakness parts of the thermal spike model were presented. In Ref. [16], Klaumünzer pointed out that it was impossible to define the temperature in such a short time and it was problem to ignore the pressure dependence of the different physical parameters of the lattice. The purpose of the present paper is not to discuss these two points in detail but to give some support to the use of the equibrium thermodynamic parameters. In addition, we have neglected the pressure dependence of these thermodynamical parameters because that may be well beyond the accuracy of current spike model.[17]

In the thermal spike model, the energy lost by slowing down of a heavy ion is imparted to the target electrons and is subsequently transferred to the lattice through electron-electron and electron-phonon interactions. This process can therefore be described by means of a set of coupled heat-diffusion equations.[18–21]

$$C_{ei}(T)\frac{\partial T_e}{\partial t}=\nabla[K_{ei}(T)\ \nabla\ T_e]+A(r,t)-g_i(T_e-T),$$

$$\rho_i C_i(T)\frac{\partial T}{\partial t}=\nabla[K_i(T)\ \nabla\ T]+g_i(T_e-T),$$

where $T_e$, $T$, $C_{ei}(T)$, $C_i(T)$, $K_{ei}(T)$, and $K_i(T)$ are the temperatures, the specific heats, and the thermal conductivities of the electronic and lattice subsystems, respectively; $g_i$ is the cou-

pling constant governing the strength of electron-phonon interaction; $\rho_i$ is the mass density of the lattice; and $i = \text{Au}, \text{SiO}_2$ represents the Au particle region and the surrounding $\text{SiO}_2$ region, respectively. $A(r,t)$ is the energy imparted to the electrons by the heavy ion at a time $t$ and a radial distance $r$ from the ion path. This takes the form[19] $A(r,t) = A_0 D(r) \exp[-(t-\tau)^2/2\tau^2]$, where $\tau$ is the mean flight time of the energy delta electrons, which is assumed to be of the order of $10^{-15}$ s. $D(r)$ is the initial spatial distribution of energy deposited on the electrons, as summarized by Waligorski et al.[22] In our case, $D(r)$ is altered to account for the presence of two materials around the ion path. $A_0$ is a normalization constant to balance the total deposited energy with that lost by the incident ion, $S_e$. $\iint A(r,t) 2\pi r dr dt = S_e$. For the insulator material $\text{SiO}_2$, we assume constant values for the specific heat and thermal conductivity of hot electrons: $C_{e\text{-silica}} \approx 1$ J/(cm$^3$ K) and $K_{e\text{-silica}} \approx 2$ J/(cm s K), following the discussion by Toulemonde et al.[20] and the references therein. The lattice specific heat $C_{\text{silica}}(T)$ is fitted to the data given in *The CRC Handbook of Chemistry and Physics*[23] for temperatures up to 273 K; data from *Perry's Chemical Engineers' Handbook*[24] are used for the temperature range from 273 K to the melting point. Above the melting point, we assume a constant specific heat, as given by Meftah et al.[18] The lattice thermal conductivity $K_{\text{silica}}(T)$ is fitted to the data for fused silica recommended in Touloukian's handbook.[25] In addition, the coupling constant $g_{\text{silica}}$ is approximated by the value for quartz, $1.25 \times 10^{13}$ W/cm$^3$/K, which is derived from an experimentally fitted mean energy-diffusion length $\lambda$ given by Ref. 20. In gold, the thermal parameters of hot electrons, $C_{e\text{-Au}}(T)$, $K_{e\text{-Au}}(T)$, and $g_{\text{Au}}$, are quite complicated, and are all temperature dependent. We use the same hypothesis as suggested by Wang et al. given by Ref. 19.[19] For lattice systems, we approximated its specific heats and thermal conductivities by that of bulk gold.

The lattice specific heat of gold, $C_{\text{Au}}(T)$, was taken from the HSC CHEMISTRY FOR WINDOWS software[26] for temperatures above 298.15 K, and fitted to the glass data given by *Perry's Chemical Engineers' Handbook*[24] for temperatures below 298.15 K. The thermal conductivity of gold, $K_{\text{Au}}(T)$, was fitted to the data recommended by Touloukian's handbook.[25] These fitted formulae are shown in Table I. It is

TABLE II. Macroscopic thermodynamical parameters of gold and $\text{SiO}_2$.

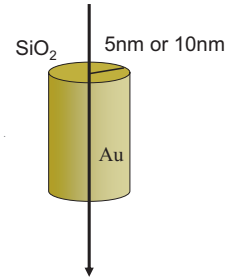| Parameters | Gold | SiO$_2$ |
| --- | --- | --- |
| Mass density [g/cm$^3$] | 19.30 (solid) | 2.62 (solid) |
| | 17.31 (liquid) | 2.32 (liquid) |
| Standard atomic weight [g/mol] | 196.9666 | 60.0843 |
| Eletron number/molecule | 79 | 30 |
| Melting temperature $T_m$ [K] | 1337.33 | 1972.0 |
| Latent heat of fusion [J/g] | 63.7164 | 142.0 |
| Boiling temperature $T_v$ [K] | 3129.0 | 3223.0 |
| Latent heat of vaporization [J/g] | 1644.95 | 4715.0 |
| Debye temperature $T_d$ [K] | 165.0 | – |



FIG. 1. (Color) Schematic model for the thermal simulation of an Au particle in $\text{SiO}_2$ matrix irradiated by a swift heavy ion.

a delicate problem to use the thermal-conductivity value of bulk gold as the lattice parameter because the heat transport of gold is dominated by its electronic part. Nevertheless, as we will see later, in the current nanoparticle case, the heat flow to the surrounding $\text{SiO}_2$ is mainly via the electron-electron coupling. Furthermore, $\text{SiO}_2$ acts as a heat insulating barrier to the gold particle. Thus, the exact value of the thermal conductivity of lattice has minor effect in the final results. Some other macroscopic thermodynamic parameters for gold and silica used in the simulation are summarized in Table II. Here we used the thermodynamical parameters of quartz as the approximations of silica because $g$ value of silica glass is unknown.

Because most of the thermodynamic parameters are temperature dependent, $A(R,t)$ is obtained numerically, and phase transformations and latent heats of both materials need to be considered, the above coupled differential equations have to be solved numerically. In implementing the computational algorithm, we used the Crank–Nicolson implicit scheme to avoid problems of convergence,[27] because the usual simple explicit iteration scheme requires a very small iteration step and thus an extremely long running time to keep the computation stable, especially in the case of metallic materials at low temperatures. In addition, we also applied the Predicator–Corrector method to improve the accuracy for large time steps.[27] By these means, we achieved a robust computation with a uniform accuracy for various materials under various conditions. Finally, we performed two-dimensional simulation. In other words, heat flow along this axis is not taken into account.

Figure 1 is a schematic model showing the configuration of the simplified two-dimensional model, in which a swift ion penetrates through the center of the cylindrical Au particle, imparting its energy to the electrons on the ion trajectory within femtoseconds (i.e., the so-called electronic-
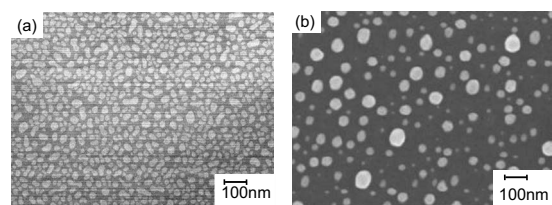


FIG. 2. SEM plan-view micrographs of Au films on $\text{SiO}_2$ after annealing at (a) 300 °C or (b) 1000 °C. Au nanoparticles were generated by the annealing process.

(a-1) before irradiation    (a-2)    50nm

(b) 110MeV Br$^{10+}$ 1 × 10$^{14}$cm$^{-2}$    (d) 100MeV Cu$^{9+}$ 1 × 10$^{14}$cm$^{-2}$

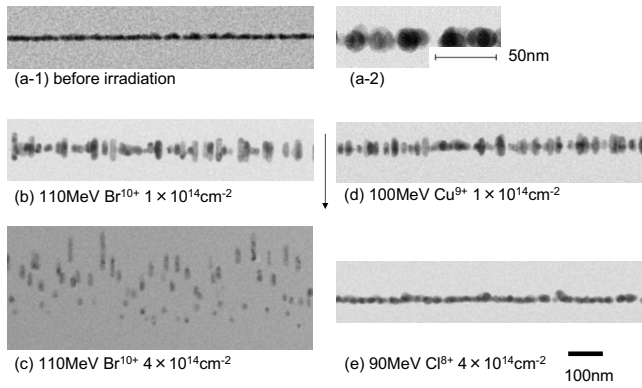(c) 110MeV Br$^{10+}$ 4 × 10$^{14}$cm$^{-2}$    (e) 90MeV Cl$^{8+}$ 4 × 10$^{14}$cm$^{-2}$    100nm

FIG. 3. Bright-field and cross-sectional TEM micrographs. Au nanoparticles were generated at 300 °C. (a-1) Pristine Au nanoparticles embedded in SiO$_2$. (a-2) Expanded view of (a-1). [(b)–(e)] Au nanoparticles in SiO$_2$ irradiated with 110 MeV Br$^{10+}$ at a fluence of 1×10$^{14}$ cm$^{-2}$ (b), 110 MeV Br$^{10+}$ at a fluence of 4×10$^{14}$ cm$^{-2}$ (c), and 100 MeV Cu$^{9+}$ at fluences of 1×10$^{14}$ cm$^{-2}$ (d), 90 MeV Cl$^{8+}$ at fluences of 4×10$^{14}$ cm$^{-2}$ (e).

stopping power regime). The energy from the resulting hot electrons diffuses to peripheral electrons by electron-electron interactions and to the lattice by electron-phonon coupling, crossing the material boundary between the surface of the Au particle and the surrounding SiO$_2$. SRIM 2003 code was used to estimate the values of the electronic and nuclear stopping powers that were used in the simulation based on the thermal spike model.[28] The electronic-stopping powers of 110 MeV Br$^{10+}$, 100 MeV Cu$^{9+}$ and 90 MeV Cl$^{8+}$ launched into Au were estimated to be 29.17, 25.30, and 12.56 keV/nm, respectively. As a comparison, the stopping powers for these ions into SiO$_2$ were estimated to be 9.203, 7.859, and 3.702 keV/nm, respectively. In high-energy ionsolid interactions, the nuclear energy loss is negligible compared with the electronic-stopping power, so we will deal with the electronic effects induced in SiO$_2$ and Au in slowing down swift heavy ions.

## III. RESULTS AND DISCUSSION

### A. SEM and TEM images

Figures 2(a) and 2(b) show SEM plan views of Au films on SiO$_2$ after annealing at 300 and 1000 °C, respectively. Note that the Au films were converted into isolated nanoparticles. The particles produced by annealing at 300 °C had an almost uniform diameter of 20 nm [Fig. 2(a)]. In contrast, the diameters of Au nanoparticles generated at 1000 °C were distributed between 20 and 80 nm. The growth of the smaller particles as the heating temperature increased can be explained in terms of Ostwald ripening.

Figure 3(a-1) shows a cross-sectional TEM view of Au nanoparticles generated at 300 °C and subsequently embedded in SiO$_2$. The 100 nm scale bar shown below and to the right of Fig. 3(e) applies to all the TEM views other than Fig. 3(a-2), which shows an expanded view with a scale bar measuring 50 nm: note that all the Au nanoparticles are embedded in the SiO$_2$ matrix. Figures 3(b) and 3(c) show Au nano-



100 nm
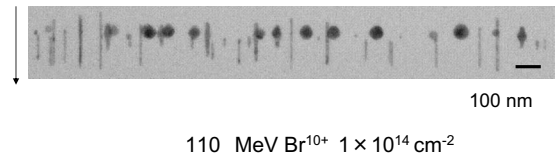
110 MeV Br$^{10+}$ 1 × 10$^{14}$ cm$^{-2}$

FIG. 4. Bright-field and cross-sectional TEM micrographs. The Au nanoparticles were generated at 1000 °C and subsequently covered by a layer of deposited SiO$_2$.

particles embedded in SiO$_2$ after irradiation with 110 MeV Br$^{10+}$ ions at fluences of 1×10$^{14}$ and 4×10$^{14}$ cm$^{-2}$, respectively. The direction of ion propagation was from the top to the bottom in the pictures, as shown by the arrow between Figs. 3(b) and 3(d). The aspect ratio of the isolated nanorods in Fig. 3(b) was estimated to be 3, but no elongation was observed in the case of some particles that touched each other. On increasing the fluence from 1×10$^{14}$ to 4 ×10$^{14}$ cm$^{-2}$ [Figs. 3(b) and 3(c), respectively], Some nanoparticles split into two or more shorter nanorods aligned end to end in the direction parallel to the ion beam. Figures 3(d) and 3(e) show Au nanoparticles embedded in SiO$_2$ after irradiation with 100 MeV Cu$^{9+}$ ions at a fluence of 1 ×10$^{14}$ cm$^{-2}$ and with 90 MeV Cl$^{8+}$ ions at a fluence of 4 ×10$^{14}$ cm$^{-2}$, respectively. The aspect ratio of the nanorods irradiated with 100 MeV Cu$^{9+}$ ions, as shown in Fig. 3(d), was estimated to be less than 2. No elongation occurred in the case of Au nanoparticles irradiated with 90 MeV Cl$^{8+}$ at a fluence of 4×10$^{14}$ cm$^{-2}$, as shown in Fig. 3(e).

Figure 4 shows a cross-sectional TEM view of nanoparticles generated at 1000 °C in SiO$_2$ and subsequently irradiated with 110 MeV Br$^{10+}$ ions at a fluence of 1 ×10$^{14}$ cm$^{-2}$. As we mentioned for Fig. 2(b), the sizes of the nanoparticles were distributed between 20 and 80 nm. Nanoparticles measuring over 50 nm in diameter were not elongated by the irradiation. The aspect ratio of the nanorods increased with decreasing diameter of the Au nanoparticles. It is also noticed that nanoparticles measuring less than 5 nm in diameter are existed and not elongated. This point will be discussed later.

### B. Simulated temperature of an Au nanorod in SiO$_2$

As a first trial of the algorithm, we compute the time evolutions of the temperatures versus time for bulk SiO$_2$ and bulk gold (Figs. 5 and Figs. 6, respectively,) when these are irradiated by a 110 MeV swift Br$^{10+}$ ion beam. In the case of SiO$_2$, as shown in Fig. 5(a), the electrons near the ion path are excited to a very high temperature in an extremely short time (of the order of a femtosecond) by the ion bombardment. Their energies are then transferred to the lattice by electron-atom interactions, and cause the lattice temperature to increase to above the melting point [Fig. 5(b)]. Here, we should emphasize that lattice temperature for times below 10$^{-13}$ s is more like a representation of the energy deposited on atoms or phonons generated, rather than the true equilibrium thermal temperature. Similarly, the melting and boiling temperatures are also not strictly correct for this short time. Of course, it is a delicate problem to use thermodynamic data
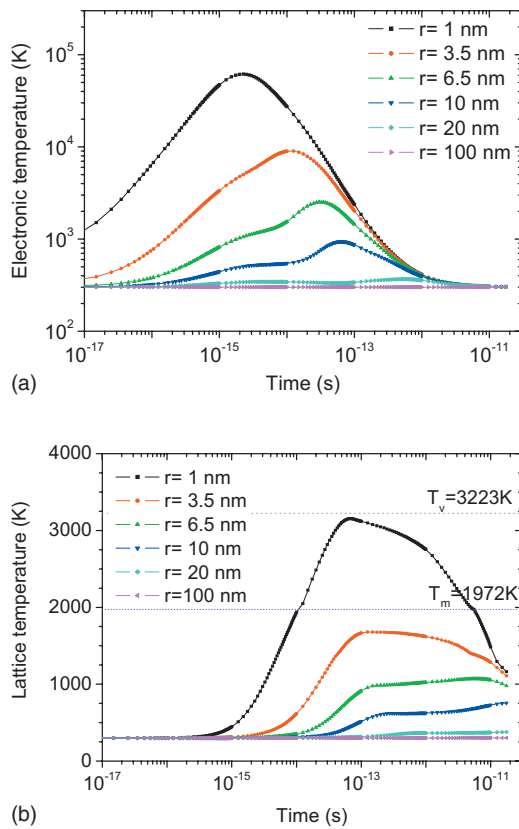
FIG. 5. (Color) The simulated evolution of the electronic temperature (a) and lattice temperature (b) versus time at various distances (1, 3.5, 6.5, 10, 20, and 100 nm) from the ion path in bulk SiO$_2$. The electronic energy-loss rate of the 110 MeV Br$^{10+}$ beam is $S_e$=9.203 keV/nm. The initial temperature of the sample is 300 K. $T_m$ and $T_v$ imply melting and vaporization temperatures, respectively.

valid for ambient pressure. However, by applying these parameters, we can roughly estimate how large radius of melting region is and gain some insights on the mechanism behind the complicated physical process.

As has been well studied previously,[18,19] a latent track may result from the rapid quenching of the molten lattice. Here, the molten region is estimated to measure about 2.65 nm from the numerical results. The present calculations for a SiO$_2$ matrix agree with published experimental results.[18] On the other hand, in the case of bulk gold, although the electronic energy-loss rate $S_e$ is even larger than that of silica, the electronic temperature does not increase much because the thermal conductivities of both the electronic subsystem and the lattice subsystems are much larger than that of silica. The heat accumulated locally before it spreads outward is insufficient to cause melting of the lattice [Fig. 6(a) and 6(b)]. No latent track should therefore be observed, and this explains why bulk gold is usually regarded as being insensitive to ion irradiation.

When we come to the gold nanoparticle embedded inside an insulating material, such as silica, the situation becomes much more complicated. Figures 7(a) and 7(b) show the calculated time evolutions of the electronic temperature for Au nanorods with radii of 5 and 10 nm, respectively, when these
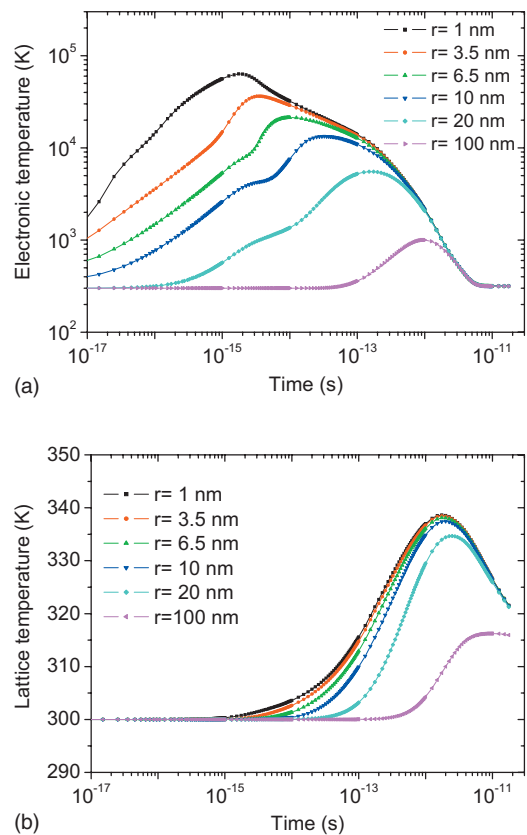


FIG. 6. (Color) The simulated evolution of the electronic temperature (a) and lattice temperature (b) versus time at various distances (1, 3.5, 6.5, 10, 20, and 100 nm) from the ion path in bulk Au. The electronic energy-loss rate of the 110 MeV Br$^{10+}$ beam is $S_e$=29.17 keV/nm. The initial temperature of the sample is 300 K.

are irradiated by the same Br$^{10+}$ ion beam as in Figs. 5 and 6. Near the gold particle, the temperature curves are steep because the hot electrons spread their energy quickly, causing an overall rapid increase in the temperature. This heat diffusion is then greatly hindered by the surrounding SiO$_2$ region, and causes the surface temperature of the nanoparticles to increase quickly. As a result, melted particles, as described in the main text, will be formed.

The results of calculated lattice temperature for Au nanorods with radii of 5 and 10 nm embedded in SiO$_2$ are given in Figs. 8(a) and 8(b), respectively; these show the evolution of the lattice temperature with time at various distances from the ion axis. For a time of less than $10^{-13}$ s, the temperature characterizes the energy imparted to the atoms. In the case of a nanorod with a radius of 5 nm, as shown in Fig. 8(a), the temperatures of the Au nanorod monitored 1 and 3.5 nm from the center are shown by black squares and red circles, respectively. 300 fs ($3 \times 10^{-13}$ s) after the ion impact, both temperatures exceed the melting point of Au (1337 K), which is shown by a black dashed line. The maximum temperatures at both distances also reach the melting point of SiO$_2$ (1992 K), which is shown by a dashed straight line. A point 6.5 nm from center of an Au nanorod of radius 5 nm is located within the SiO$_2$ matrix. The temperature at this point increases dramatically 5 fs ($5 \times 10^{-15}$ s) after ion impact, and exceeds the melting point of SiO$_2$ for the period between
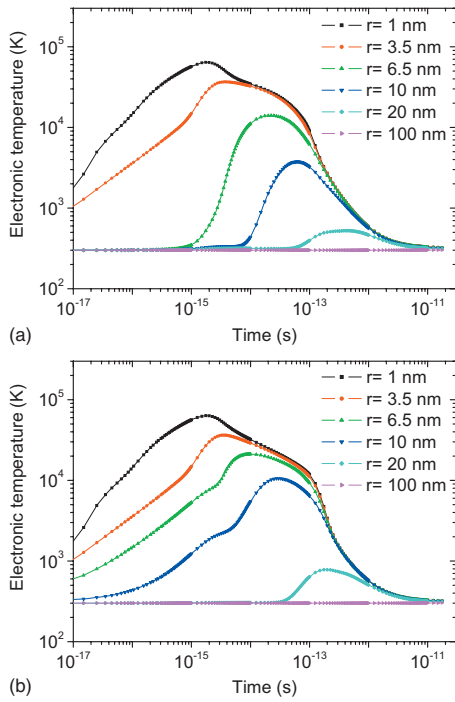
FIG. 7. (Color) The simulated evolution of the electronic temperature versus time at various distances (1, 3.5, 6.5, 10, 20, and 100 nm) from the ion path when a 110 MeV $Br^{10+}$ ion penetrates the center of an Au particle embedded in $SiO_2$. The radii of the Au nanoparticles are 5 nm (a) and 10 nm (b). The initial temperature of the sample is 300 K.
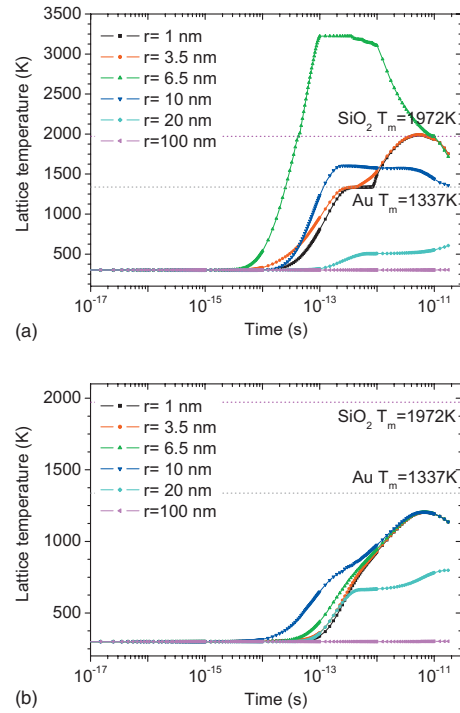


FIG. 8. (Color) The calculated lattice temperature versus time at distances of 1, 3.5, 6.5, 10, 20, and 100 nm from the ion path. (a) 5-nm-radius Au nanoparticle embedded in $SiO_2$. (b) 10-nm-radius Au nanoparticle embedded in $SiO_2$. The sample is at 300 K. The melting temperatures of $SiO_2$ and Au are shown in the figures.

20 fs and 10 ps after the ion impact. The lattice temperature 10 nm from the center of the nanoparticle does not exceed the melting point of $SiO_2$. In other words, $SiO_2$, as well as Au, is melted for 10 ps in the region within 10 nm of the center of the nanoparticle.

Here we should explain why the silica temperature increases before that of the Au nanoparticle even though the incident ion energy is deposited in the Au nanoparticle and subsequently coupled to the silica matrix. The electrons at ion path respond instantaneously to the penetrating ion, resulting in a quick rising in the electronic temperature as shown in Fig. 7(a) and 7(b). These hot electrons within Au then diffuse their energy rapidly to electrons of outside silica and cause their temperature to be raised correspondingly. Because the electron-lattice coupling constant of silica is larger than that of Au ($\sim 10^{13}$ $W/cm^3/K$ vs $\sim 10^{10}$ $W/cm^3/K$) while its conductivity is smaller, we observed in the simulation that the silica lattice temperature increases ahead of the inner Au particle, and thus will feed the heat back to the particle by phonon-phonon interactions [Fig. 8(a)].

A plot of the lattice temperature of an Au nanorod with a radius of 10 nm in $SiO_2$ against the time is shown in Fig. 8(b). Note that temperatures for points 1 to 100 nm from the center of ion are shown in the figure. At no point does the temperature reach to the melting point of either $SiO_2$ or Au. We conclude that small Au nanoparticles and $SiO_2$ close to the 5 nm Au nanoparticles are simultaneously melted by ion bombardment in simulated results based on thermal spike model. In real world, however, Au nanoparticles whose radii
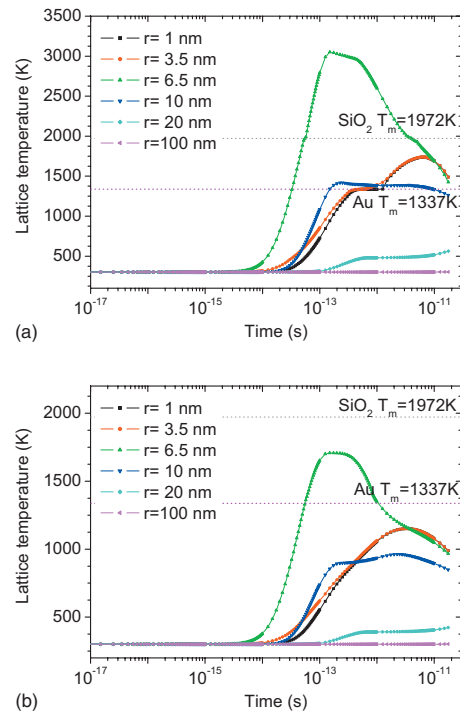


FIG. 9. (Color) The calculated lattice temperature versus time at distances of 1, 3.5, 6.5, 10, 20, and 100 nm from the ion path. Radius of Au nanoparticle embedded in $SiO_2$ is 5 nm. (a) 100 MeV $Cu^{9+}$ ion. (b) 90MeV $Cl^{8+}$ ion. The sample is at 300 K. The melting temperatures of $SiO_2$ and Au are shown in the figures.

are less than 25 nm are elongated with irradiation from the experimental results as depicted in Fig. 4. The radii in the experiments do not match exactly with those obtained in the calculation because of the inherent limitations of current spike model as well as the uncertainty of the input parameters. Nevertheless, we can conclude that lattice temperature of small size Au nanoparticles increase much higher than lattice temperature of large size nanoparticles. In Fig. 3(b), some particles that were close to each other were not elongated with irradiation. Such particles can be recognized as large size particles. This experimental result can also be explained with the present simulation.

Figure 9(a) shows the lattice temperature against time at distances of 1, 3.5, 6.5, 10, 20, and 100 nm from a 100 MeV $Cu^{9+}$ ion interacting with a 5 nm radius Au rod embedded in $SiO_2$; Fig. 9(b) shows the corresponding figures for a 90 MeV $Cl^{8+}$ ion. The temperature exceeds the melting point of Au at points 1 and 3.5 nm from the Au nanorod in the former case [Fig. 9(a)]. The temperature at a point 6.5 nm away, located in $SiO_2$, reaches 3000 K, which is above the melting point of $SiO_2$ (1972 K). Temperatures at points 10, 20, and 100 nm away remain below the melting point of $SiO_2$. Therefore, both the Au nanorod and the surrounding $SiO_2$ are melted by the passage of a 100 MeV $Cu^{9+}$ ion. In Fig. 9(b), the temperatures at distances of both 1 and 3.5 nm, which are located in the Au rod, remain below the melting point of Au; similarly, the temperatures at 6.5, 10, 20, and 100 nm remain below the melting temperature of $SiO_2$. Therefore, neither the Au nor the $SiO_2$ is melted by the passage of a 90 MeV $Cl^{8+}$ ion. In the cross-sectional TEM views of Au nanoparticles in $SiO_2$ irradiated by 100 MeV $Cu^{9+}$ and 900 MeV $Cl^{8+}$ ions, the Au nanoparticles showed elongation by 100 MeV $Cu^{9+}$, whereas no elongation was found for 90 MeV $Cl^{8+}$. These experimental results agreed well with the simulation.

The lattice temperature of Au nanorods in $SiO_2$ can be estimated by using the thermal spike method. The simulation shows that when the temperatures of both Au and $SiO_2$ exceed their respective melting temperatures, the Au nanoparticles become elongated. The temperature evolution does not in itself give a complete explanation of the mechanism of elongation of Au. It has been reported that the rapid thermal expansion of the ion track results in large shear stresses in the heated region.[29,30] This usually holds for a homogeneous system, but we presumed that it may also hold for the inhomogeneous system. As a result, the compressive radial stress increases and the compressive axial stress decreases during viscous flow.[29,30] The effects of stress and the thermal spike combine to induce the elongation of the Au nanoparticles.

We need to discuss why nanoparticles measuring less than 5 nm in diameter are existed and not elongated, as is shown in Fig. 4. It has been reported that the system evolves toward the growth of large particles and the dissolution of smaller ones in conventional Ostwald ripening with increasing irradiation temperature.[12] In contrast, below a critical temperature, the particle sizes decreased on irradiation as a result of inverse Ostwald ripening. Inverse Ostwald ripening was also observed under a high ion flux. The small particles shown in Fig. 4 may have originated from minority part of the Ostwald ripening under the high ion flux.

## IV. CONCLUSION

We examined the unique features of Au nanoparticles in $SiO_2$ irradiated by swift heavy ions. Elongation of Au nanoparticles was observed in the case of nanoparticles with a diameter of less than 25 nm. The mechanism of this elongation is explained well by using the thermal spike model. As a next step, we will perform the simulation based on the Coulomb explosion model to compare the present data used in the thermal spike model. We believe that Au nanorods aligned in the direction of ion propagation could be fabricated by irradiation with swift heavy ions. In the near feature, this method could be used to produce plasmonic optical devices.

*Author to whom correspondence should be addressed. k.awazu@aist.go.jp. FAX: +81(29)861-2939.

[1] N. Halas, MRS Bull. **30**, 362 (2005).

[2] C. J. Murphy, T. K. Sau, A. Gole, and C. J. Orendorff, MRS Bull. **30**, 349 (2005).

[3] Y. Xia and N. J. Halas, MRS Bull. **30**, 338 (2005).

[4] S. Eustis and M. A. El-Sayed, Chem. Soc. Rev. **35**, 209 (2006).

[5] S. Roorda, T. V. Dillen, A. Polman, C. Graf, A. V. Blaaderen, and B. J. Kooi, Adv. Mater. (Weinheim, Ger.) **16**, 235 (2004).

[6] C. Harkati Kerboua, J.-M. Lamarre, L. Martinu, and S. Roorda, Nucl. Instrum. Methods Phys. Res. B **257**, 42 (2007).

[7] G. Rizza, Y. Ramjauny, T. Gacoin, and S. Henry, Nucl. Instrum. Methods Phys. Res. B **257**, 15 (2007).

[8] G. Rizza, Y. Ramjauny, T. Gacoin, L. Vieille, and S. Henry, Phys. Rev. B **76**, 245414 (2007).

[9] G. Rizza, H. Cheverry, T. Gacoin, A. Lamasson, and S. Henry, J. Appl. Phys. **77**, 014321 (2003).

[10] Y. K. Mishra, D. K. Avasthi, P. K. Kulriya, F. Singh, D. Kabiraj, A. Tripathi, J. C. Pivin, I. S. Bayer, and A. Biswas, Appl. Phys. Lett. **90**, 073110 (2007).

[11] Y. K. Mishra, F. Singh, D. K. Avasthi, J. C. Pivin, D. Malinovska, and E. Pippel, Appl. Phys. Lett. **91**, 063103 (2007).

[12] K. H. Heinig, T. Müller, B. Schmidt, M. Strobel, and W. Möller, Appl. Phys. A: Mater. Sci. Process. **77**, 17 (2003).

[13] C. D'Orléans, C. Cerruti, C. Estournès, J. J. Grob, J. L. Guille, F. Haas, D. Muller, M. Richard-Plouet, and J. P. Stoquert, Nucl. Instrum. Methods Phys. Res. B **209**, 316 (2003).

[14] B. Schmidt, A. Mücklich, L. Röntzsch, and K.-H. Heinig, Nucl.

Instrum. Methods Phys. Res. B **257**, 30 (2007).

[15] M. Toulemonde, Mat. Fys. Medd. K. Dan. Vidensk. Selsk. **52**, 263 (2006).

[16] S. Klaumünzer, Mat. Fys. Medd. K. Dan. Vidensk. Selsk. **52**, 293 (2006).

[17] M. Toulemonde, C. Dufour, and E. Paumier, Phys. Rev. B **46**, 14362 (1992).

[18] A. Meftah, F. Brisard, J. M. Constantini, E. Dooryhee, M. Hage-Ali, M. Hervieu, J. P. Stoquert, F. Studer, and M. Toulemonde, Phys. Rev. B **49**, 12457 (1994).

[19] Z. G. Wang, C. Dufour, E. Paumier, and M. Toulemonde, J. Phys.: Condens. Matter **6**, 6733 (1994).

[20] M. Toulemonde, E. Paumier, J. M. Costantini, Ch. Dufour, A. Meftah, and F. Studer, Nucl. Instrum. Methods Phys. Res. B **116**, 37 (1996).

[21] M. Toulemonde, C. Dufour, A. Meftah, and E. Paumier, Nucl. Instrum. Methods Phys. Res. B **166-167**, 903 (2000).

[22] M. P. R. Waligorski, R. N. Hamm, and R. Katz, Nucl. Tracks Radiat. Meas. **11**, 309 (1986).

[23] D. R. Lide, *CRC Handbook of Chemistry and Physics, A Ready-Reference Book of Chemical and Physical Data*, 86th ed. (CRC, Boca Raton, 2006).

[24] R. H. Perry and D. W. Green, *Perry's Chemical Engineers' Handbook*, 6th ed. (McGraw-Hill, New York, 1984).

[25] Y. S. Touloukian, R. W. Powell, and C. Y. Ho, *Thermophysical Properties of Matter* (IFI/Plenum, New York, 1970). For fused silica, Vol. 2, Thermal Conductivity: Nonmetallic Solids, p. 193. For gold, Vol. 1, Thermal Conductivity: Metallic Elements and Alloys, p. 137.

[26] HSC Chemistry for Windows, version 5.1, ESM Software, 2005.

[27] W. F. Ames, *Numerical Methods for Partial Differential Equations*, 2nd ed. (Academic, Boston, 1977), p. 82.

[28] http://www.srim.org/SRIM/SRIM2003.htm

[29] H. Trinkaus and A. I. Ryazanov, Phys. Rev. Lett. **74**, 5072 (1995).

[30] T. van Dillen, A. Polman, P. R. Onck, and E. van der Giessen, Phys. Rev. B **71**, 024103 (2005).